

# Rational Design of Hierarchical “Ceramic-in-Polymer” and “Polymer-in-Ceramic” Electrolytes for Dendrite-Free Solid-State Batteries

Hanyu Huo, Yue Chen, Jing Luo, Xiaofei Yang, Xiangxin Guo,\* and Xueliang Sun\*

Solid polymer electrolytes as one of the promising solid-state electrolytes have received extensive attention due to their excellent flexibility. However, the issues of lithium (Li) dendrite growth still hinder their practical applications in solid-state batteries (SSBs). Herein, composite electrolytes from “ceramic-in-polymer” (CIP) to “polymer-in-ceramic” (PIC) with different sizes of garnet particles are investigated for their effectiveness in dendrite suppression. While the CIP electrolyte with 20 vol% 200 nm  $\text{Li}_{6.4}\text{La}_3\text{Zr}_{1.4}\text{Ta}_{0.6}\text{O}_{12}$  (LLZTO) particles (CIP-200 nm) exhibits the highest ionic conductivity of  $1.6 \times 10^{-4} \text{ S cm}^{-1}$  at 30 °C and excellent flexibility, the PIC electrolyte with 80 vol% 5  $\mu\text{m}$  LLZTO (PIC-5  $\mu\text{m}$ ) shows the highest tensile strength of 12.7 MPa. A sandwich-type composite electrolyte (SCE) with hierarchical garnet particles (a PIC-5  $\mu\text{m}$  interlayer sandwiched between two CIP-200 nm thin layers) is constructed to simultaneously achieve dendrite suppression and excellent interfacial contact with Li metal. The SCE enables highly stable Li plating/stripping cycling for over 400 h at 0.2 mA  $\text{cm}^{-2}$  at 30 °C. The  $\text{LiFePO}_4/\text{SCE}/\text{Li}$  cells also demonstrate excellent cycle performance at room temperature. Fabricating sandwich-type composite electrolytes with hierarchical filler designs can be an effective strategy to achieve dendrite-free SSBs with high performance and high safety at room temperature.

## 1. Introduction

Next-generation rechargeable Li-ion batteries (LIBs) have to fulfill the increasing demand of high power and energy storage densities.<sup>[1]</sup> Lithium (Li) metal is regarded as the “Holy Grail” due to its high theoretical capacity (3860 mAh  $\text{g}^{-1}$ ), low negative electrochemical potential (−3.04 V vs the standard hydrogen electrode), and light weight (0.53 g  $\text{cm}^{-3}$ ). Li metal anodes have received extensive research attentions, particularly for applications in high-energy-density Li–sulfur (Li–S) and Li–oxygen (Li–O<sub>2</sub>) batteries.<sup>[2,3]</sup> However, the vulnerable and inhomogeneous solid electrolyte interface at the Li metal interface can lead to serious Li dendrite growth during repeated Li plating-stripping cycles, and thus low Coulombic efficiency, poor cycle life, and safety concerns.<sup>[4]</sup>

Solid-state batteries (SSBs) show significant advantages over traditional liquid electrolyte based LIBs. The large electrochemical window of solid-state

electrolytes (SSEs) can enable the use of Li metal anodes and high-voltage cathodes, rendering a high energy density for SSBs. In addition, the flammability and leakage concerns related to the conventional liquid electrolytes are eliminated by replacing with SSEs.<sup>[5]</sup> Despite of these beneficial intrinsic properties, practical SSEs should meet the following requirements to ensure good electrochemical performance for SSBs:<sup>[3]</sup> (1) ionic conductivity above  $10^{-4} \text{ S cm}^{-2}$  at room temperature, (2) stable and robust interface between SSEs and electrodes for smooth  $\text{Li}^+$  transport,<sup>[6]</sup> and (3) mechanically strong and flexible to suppress Li dendrite growth and allow ease of handling.


As a group of promising SSE candidates, solid polymer electrolytes (SPEs) have been studied for decades since the demonstration of  $\text{Li}^+$  conduction in poly(ethylene oxide) (PEO) polymer complexes with alkali metal salts.<sup>[7]</sup> Various approaches were employed to improve the ionic conductivities of SPEs at room temperature, including polymer bending,<sup>[8]</sup> grafting short oligomers onto the polymer backbone,<sup>[9]</sup> adding ionic liquids or plasticizers,<sup>[10]</sup> and doping inorganic or metal–organic frameworks fillers.<sup>[11]</sup> Recently, various solid electrolyte particles such as  $\text{Li}_{6.4}\text{La}_3\text{Zr}_{1.4}\text{Ta}_{0.6}\text{O}_{12}$  (LLZTO) or  $\text{Li}_{1.5}\text{Al}_{0.5}\text{Ge}_{1.5}(\text{PO}_4)_3$

Dr. H. Huo, Dr. Y. Chen  
State Key Laboratory of High Performance Ceramics  
and Superfine Microstructure  
Shanghai Institute of Ceramics  
Chinese Academy of Sciences  
Shanghai 200050, China

Dr. H. Huo, Dr. Y. Chen  
Center of Materials Science and Optoelectronics Engineering  
University of Chinese Academy of Sciences  
Beijing 100049, China

Dr. H. Huo, Dr. J. Luo, Dr. X. Yang, Prof. X. Sun  
Department of Mechanical and Materials Engineering  
University of Western Ontario London  
Ontario N6A 5B9, Canada  
E-mail: xsun9@uwo.ca

Prof. X. Guo  
College of Physics  
Qingdao University  
Qingdao 266071, China  
E-mail: xxguo@qdu.edu.cn

 The ORCID identification number(s) for the author(s) of this article can be found under <https://doi.org/10.1002/aenm.201804004>.

DOI: 10.1002/aenm.201804004

(LAGP) have been dispersed in the polymer matrix to enhance the conductivity.<sup>[12–14]</sup> In our previous work, SPEs consisting of PEO and LLZTO particles with different sizes from 40 nm to 10  $\mu\text{m}$  were fabricated.<sup>[12]</sup> Even though much progress has been achieved in terms of ionic conductivity, the Li dendrite issue and susceptible penetration through such “ceramic-in-polymer” (CIP) electrolytes can cause short circuit in SSBs, seriously hindering practical applications. SSEs with a shear modulus more than twice that of the metallic Li ( $\approx 3.4$  GPa) can theoretically act as mechanical barriers for suppressing Li dendrites.<sup>[15]</sup> However, a high modulus is difficult to achieve in SPEs and can lead to alternative contact issues with the electrodes.<sup>[16]</sup> Poor interfacial contacts between SSEs and electrodes often cause large interfacial resistance and overpotential during the charge–discharge cycles, thus poor electrochemical performance of the subjected SSBs.<sup>[17]</sup> Therefore, it is critical to find a balance between the mechanical strength and flexibility to simultaneously achieve Li dendrite suppression and low interfacial resistance.<sup>[18]</sup>

Herein, the effectiveness of Li dendrite suppression using composite electrolytes from “ceramic-in-polymers” (CIPs) to “polymer-in-ceramics” (PICs) was systematically investigated. While CIPs with smaller LLZTO particles showed higher ionic conductivities, PICs with larger LLZTO particles exhibited higher mechanical strengths. The results showed that the capability of Li dendrite suppression directly depended on the mechanical strength of electrolytes at an elevated temperature, but the room-temperature compatibility with Li metal was limited by the interfacial flexibility. Therefore, a sandwich-type composite electrolyte (SCE) was rationally designed with a mechanically strong PIC interlayer and flexible CIP outer

layers. Such SCE with hierarchical garnet particles can successfully achieve both dendrite suppression and excellent interfacial contact with electrodes. Solid-state Li symmetrical cells and the  $\text{LiFePO}_4$  (LFP)/Li full cells using our designed SCE demonstrated excellent electrochemical performance at room temperature.

## 2. Results and Discussion

The microscale LLZTO powders were obtained by solid-state reactions and exhibited pure cubic garnet structure with good crystallinity (Figure S1, Supporting Information).<sup>[19]</sup> Figure S2a (Supporting Information) shows the particle size distribution of the as-prepared LLZTO particles that has a  $D_{50}$  of 5.1  $\mu\text{m}$ .<sup>[20]</sup> Scanning electron microscopy (SEM) showed the morphology of the LLZTO particles and confirmed the apparent size of  $\approx 5$   $\mu\text{m}$  (Figure 2Sb, Supporting Information). After dry ball milling in an Ar atmosphere, the LLZTO particles remained a pure garnet structure but a decreased size to  $\approx 200$  nm (Figure S2c,d, Supporting Information).

The composite electrolytes with various concentration (20, 50, and 80 vol%) and different particle sizes (200 nm and 5  $\mu\text{m}$ ) of LLZTO were fabricated by blade casting. As shown in Figure 1a,b, the composite electrolytes with 20 vol% LLZTO particles (either 200 nm or 5  $\mu\text{m}$ ) exhibited typical “ceramic-in-polymer” characteristics, where a small amount of ceramic particles were well distributed in the PEO polymer matrix. We abbreviate them as CIP-200 nm and CIP-5  $\mu\text{m}$ , respectively. When increasing the concentration of LLZTO to 80 vol%, LLZTO particles became the majority and the PEO

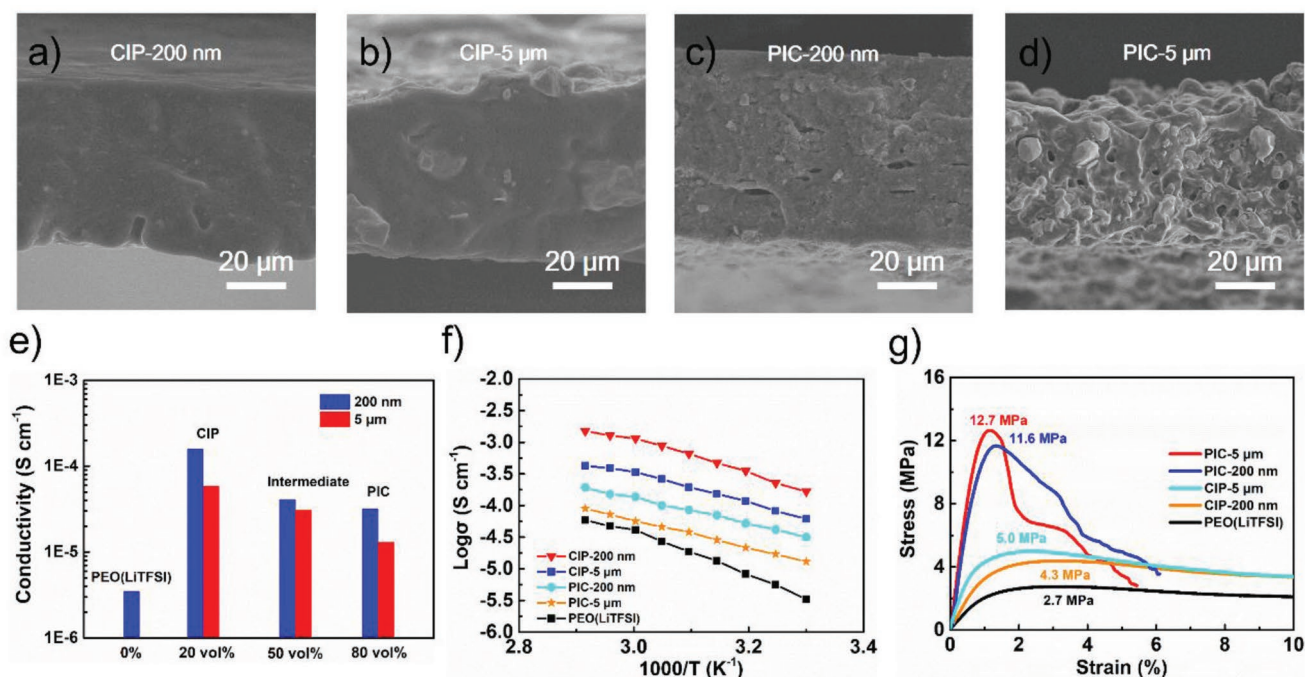


**Figure 1.** The cross-sectional SEM images of a) CIP-200 nm, b) CIP-5  $\mu\text{m}$ , c) PIC-200 nm, and d) PIC-5  $\mu\text{m}$  (a small amount of LLZTO particles were well distributed in the PEO polymer matrix for CIPs, while PEO polymer was filling in the gaps of ceramic particles for PICs). e) The conductivities at 30 °C, f) Arrhenius plots, and g) stress–strain curves of the different composite electrolytes.

polymer was filling in the gaps of them (Figure 1c,d). These two “polymer-in-ceramic” electrolytes are denoted as PIC-200 nm and PIC-5  $\mu\text{m}$ . The composite electrolytes with 50 vol% LLZTO particles were in the transition between “ceramic-in-polymer” and “polymer-in-ceramic” (Figure S3, Supporting Information). The thicknesses of all composite electrolytes are  $\approx 60 \mu\text{m}$ . The conductivities of these composite electrolytes were characterized by electrochemical impedance spectroscopy (EIS). The PEO(LiTFSI) electrolyte showed an ionic conductivity of  $3.5 \times 10^{-6} \text{ S cm}^{-1}$  at 30 °C (Figure 1e; Figure S4a, Supporting Information). As shown in Figure 1f, all composite electrolytes exhibited higher ionic conductivities than the pure PEO(LiTFSI) in a wide temperature range from 30 to 70 °C. In addition, the CIP electrolytes generally had higher ionic conductivities than the PIC electrolytes, and the composite electrolytes with smaller LLZTO fillers exhibited higher ionic conductivities. An optimal conductivity of  $1.6 \times 10^{-4} \text{ S cm}^{-1}$  was achieved by CIP-200 nm at 30 °C (Figure 1e).

The observed ionic conductivities from CIPs to PICs were interrelated with the interactions between the PEO matrix and the LLZTO fillers. Considering CIPs, the small amount of LLZTO particles can decrease the crystallinity of the PEO matrix, yielding an increasing free volume for the PEO segmental motions.<sup>[21]</sup> The  $\text{Li}^+$  can not only hop through the polymer segments but also move along the interface between the PEO chains and LLZTO particles due to the percolation effect.<sup>[22]</sup> However, when the amount of LLZTO surpassed the percolation threshold, the interfacial  $\text{Li}^+$  channels were interfered and in turn led to decrease in ionic conductivity. Further increasing the LLZTO content to PICs, the accumulated filler particles could hinder the PEO segmental motions and reduce ionic conductivity in the polymer region.  $\text{Li}^+$  tended to migrate via the discrete LLZTO particles in PICs, providing a lower conductivity than that of the CIPs.<sup>[23]</sup> For example, the conductivity of PIC-200 nm is  $3.2 \times 10^{-5} \text{ S cm}^{-1}$  at 30 °C, one order of magnitude smaller than that of CIP-200 nm (Figure 1f). In addition, the 200 nm LLZTO particles showed an advantage over the 5  $\mu\text{m}$  ones as fillers to enhance ionic conductivity. This size effect is consistent with our previous work (Figure 1f; Figure S4, Supporting Information).<sup>[12]</sup> For example, the CIP-200 nm exhibited a higher ionic conductivity of  $8.7 \times 10^{-4} \text{ S cm}^{-1}$  than CIP-5  $\mu\text{m}$  of  $2.6 \times 10^{-4} \text{ S cm}^{-1}$  at 55 °C (Figure 1f). The trends were valid over a temperature range from 30 to 70 °C. The temperature dependent ionic conductivities fitted well with the Arrhenius behavior (Figure S5, Supporting Information). Even though the CIP electrolytes showed higher ionic conductivities than the PIC electrolytes, the PIC electrolytes generally had smaller activation energies than the CIP electrolytes mainly caused by the different  $\text{Li}^+$  transport pathways.

The LLZTO ceramic possessed a shear modulus up to 55 GPa, which far exceeds the minimum value ( $\approx 8.5 \text{ GPa}$ ) required to suppress the Li dendrite propagation.<sup>[24]</sup> Adding LLZTO as a filler was expected to enhance the mechanical strength of the composite electrolytes to suppress dendrites as a physical barrier. Figure 1g details the correlation between the LLZTO content and the tensile strength of the composite electrolytes. The tensile strength of pure PEO(LiTFSI) was merely 2.7 MPa, as consistent with previous studies.<sup>[25]</sup> Upon addition of LLZTO, the tensile strength was directly related to

the amount of LLZTO. The tensile strength substantially increased from 4.3–5.0 MPa of CIPs to 11.6–12.7 MPa of PICs. A larger filler size at the same volumetric concentration also led to a slightly mechanically stronger composite electrolyte, as the tensile strength were 5.0 versus 4.3 MPa for CIP-5  $\mu\text{m}$  and CIP-200 nm and 12.7 versus 11.6 MPa for PIC-5  $\mu\text{m}$  and PIC-200 nm. The resulted PIC-5  $\mu\text{m}$  was almost five times stronger than the pure PEO(LiTFSI) electrolyte.

Symmetric Li cells constructed with different composite electrolytes were assembled in order to investigate their dendrite suppressing capabilities. Note that the cycle performances were performed at 55 °C to decrease the influence caused by the different interfacial conditions.<sup>[26]</sup> As shown in Figure S6 (Supporting Information), the PEO(LiTFSI) cell was short circuited soon after 68 h of cycling under  $0.2 \text{ mA cm}^{-2}$  ( $0.1 \text{ mAh cm}^{-2}$ ). Depending on the mechanical strength enhancement of different CIPs and PICs, cells using these electrolytes exhibited different extension on cycle life under the same testing conditions. The CIP-200 nm and CIP-5  $\mu\text{m}$  electrolytes showed limited improvements and short circuited after 130 and 183 h cycling, respectively (Figure 2). As SEM images shown in Figure 3a,b, the surface of Li metal anodes collected from the short-circuit cells exhibited mossy-like dendrite morphologies. By contrast, the mechanically strong PIC-5  $\mu\text{m}$  electrolyte enabled stable cycling for 600 h. The cell with the slightly mechanically weaker PIC-200 nm was short circuited after 473 h cycling (Figure 2). A dendrite-free morphology was observed on the Li electrode from the PIC-5  $\mu\text{m}$  cell in comparison with that from the PIC-200 nm cell (Figure 3c,d). We infer that the mechanically strong PIC electrolytes can effectively suppress Li dendrites. As an intermediate between CIP and PIC, the electrolytes with 50 vol% LLZTO also exhibited cycling performance in between CIPs and PICs (Figure S6, Supporting Information). Similarly, the mossy-like dendrites were observed on the Li metal surface using the intermediate electrolytes (Figure S7, Supporting Information). Under a low current density of  $0.1 \text{ mA cm}^{-2}$  ( $0.05 \text{ mAh cm}^{-2}$ ), both PIC-200 nm and PIC-5  $\mu\text{m}$  cells demonstrated stable cycling performance for over 800 h without obvious voltage change, indicating favorable Li plating/stripping behaviors (Figure S8, Supporting Information).

According to the Li plating/stripping cycling performance, the cycle life of cells using different composite electrolytes was directly related to the mechanical strength of the electrolytes instead of their ionic conductivities. As demonstrated earlier, when increasing the LLZTO concentration from CIP to PIC, the mechanical strength of the composite electrolytes increased from  $\approx 5$  to  $\approx 12 \text{ MPa}$ . At the same LLZTO concentration, the larger LLZTO particle size (5  $\mu\text{m}$  vs 200 nm) led to stronger mechanical properties. The larger mechanical strength of electrolytes contributed to a better dendrite suppressing capability,<sup>[15]</sup> as consistent with the trend of cycling performance. Figure 3e proposes schematic illustrations to explain Li dendrite growth behaviors in CIPs and PICs with different LLZTO sizes. The polymer matrix as the soft component of the composite electrolytes are more susceptible to Li dendrite penetration, causing a short circuit of working battery. The CIP electrolytes, no matter with 200 nm or 5  $\mu\text{m}$  LLZTO, have a large volume of connected PEO matrix with dilute dispersion



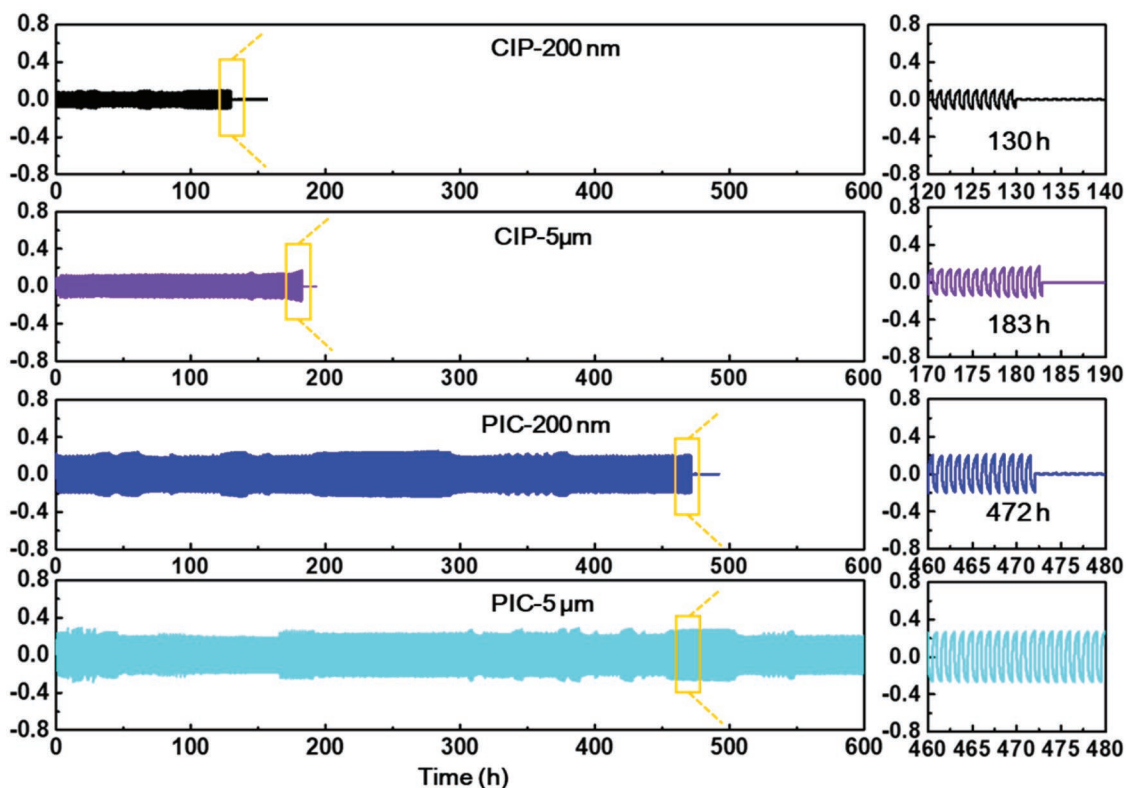


**Figure 2.** The voltage profiles of Li symmetrical cells with composite electrolytes from CIPs to PICs. The voltage profiles were obtained from galvanostatic cycles at a current density of  $0.2 \text{ mA cm}^{-2}$  with 0.5 h stripping-0.5 h plating alternating steps at  $55 \text{ }^\circ\text{C}$ .

of LLZTO. Once Li dendrite growth was initiated, the dendrites can bypass the rigid LLZTO particles and continuously grow along the PEO region until short circuit. In PIC electrolytes, the large concentration of LLZTO particles with ultrahigh

modulus hinder the propagation of Li dendrites. However, the smaller 200 nm LLZTO is more dispersive in the PEO matrix than the larger  $5 \mu\text{m}$  LLZTO, the PEO matrix in PIC-200 nm can be partially connected, providing pathways for Li dendrite

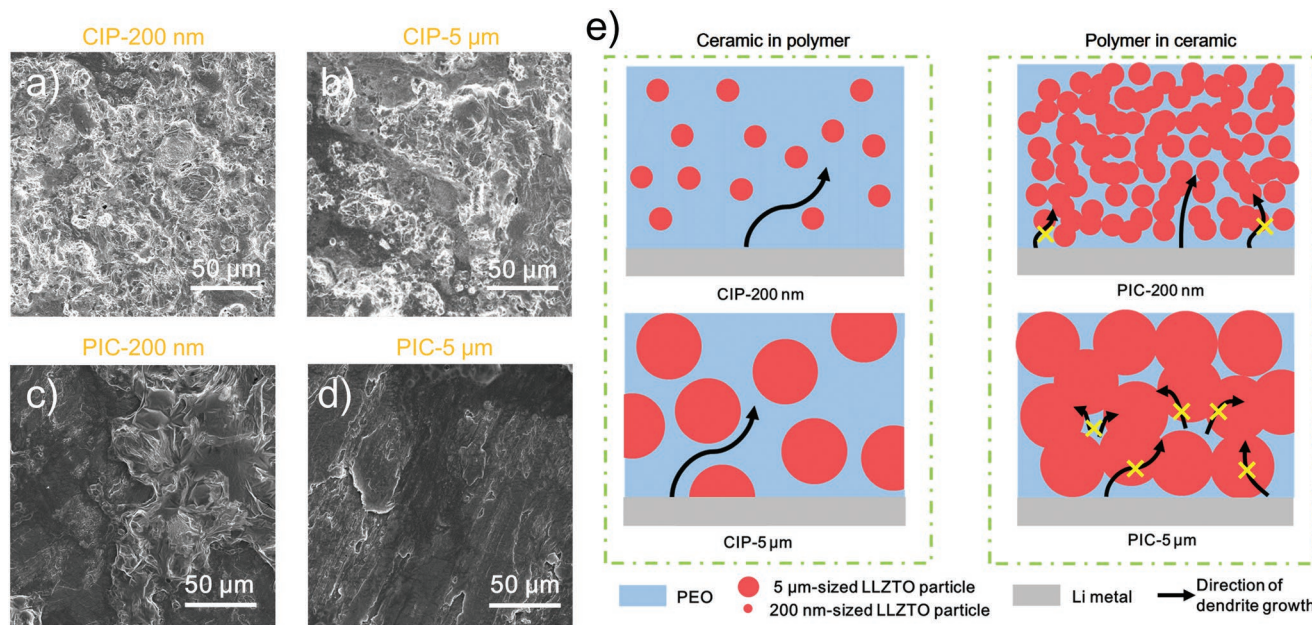


**Figure 3.** Typical SEM images of Li metal anodes after short circuit with a) CIP-200 nm, b) CIP- $5 \mu\text{m}$ , c) PIC-200 nm electrolyte cycling under  $0.2 \text{ mA cm}^{-2}$  ( $0.1 \text{ mAh cm}^{-2}$ ) at  $55 \text{ }^\circ\text{C}$ . d) SEM image of Li metal anode with PIC- $5 \mu\text{m}$  after 600 h cycles under  $0.2 \text{ mA cm}^{-2}$  at  $55 \text{ }^\circ\text{C}$ . e) The schematic illustrations of possible dendrite growth in different composite electrolytes.

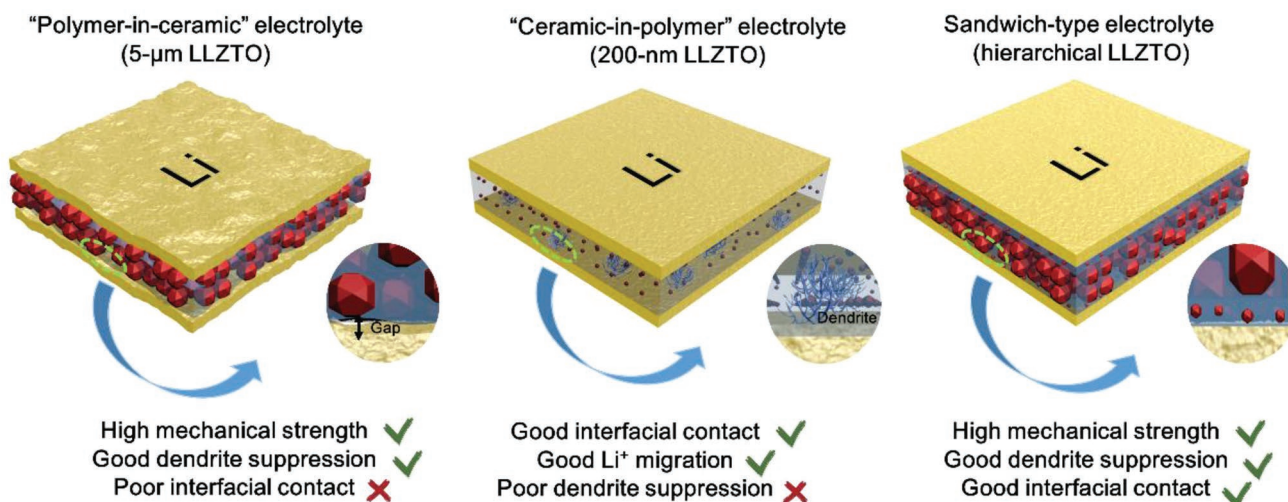


**Figure 4.** The schematic illustration of the PIC-5  $\mu\text{m}$ , CIP-200 nm, and hierarchical sandwich-type composite electrolytes.

propagation. That was probably the reason for the short circuit of the CIP-200 nm cell at a high current density. By contrast, the larger 5  $\mu\text{m}$  LLZTO particles in PIC-5  $\mu\text{m}$  may disrupt and isolate the PEO matrix, mechanically blocking Li dendrite growth and extending the cycle life.

Unlike operations at an elevated temperature with quasi-molten PEO matrix, the rough surface of the PIC-5  $\mu\text{m}$  electrolyte can cause a poor contact with Li anode at room temperature. In order to justify the room-temperature performance for practical applications, we propose a sandwich-type composite electrolyte (SCE) with hierarchical LLZTO particles (Figure 4). A PIC-5  $\mu\text{m}$  layer is designed to be sandwiched between two CIP-200 nm layers. The PIC-5  $\mu\text{m}$  middle layer is mechanically strong to suppress Li dendrites, and the CIP-200 nm layers are flexible and highly ionic conductive ( $1.6 \times 10^{-4} \text{ S cm}^{-1}$  at 30  $^{\circ}\text{C}$ ) to ensure good interfacial properties with electrodes. In addition, the CIP-200 nm layer showed a high  $\text{Li}^+$  transference number ( $t_+$ ) of 0.47 (Figure S9, Supporting Information), which can also immobilize anions and guide a uniform distribution of electrical field.<sup>[14]</sup>

As shown in Figure 5a,b, the SCE was fabricated using the doctor blade method layer by layer.<sup>[12,27]</sup> The as-obtained SCE is freestanding and flexible (Figure 5c). The cross-sectional SEM image in Figure 5d shows a clear hierarchical structure, where garnet particles with different sizes (200 nm and 5  $\mu\text{m}$ ) and contents (20 and 80 vol%) were orderly dispersed in the polymer matrix. The PIC-5  $\mu\text{m}$  interlayer of  $\approx 40 \mu\text{m}$  was sandwiched between two CIP-200 nm thin layers (10  $\mu\text{m}$ ). As shown in Figure 5e, a rough morphology with humps of microscale LLZTO particles were observed at the surface of the PIC-5  $\mu\text{m}$  layer. The rocky surface of PIC-5  $\mu\text{m}$  was confirmed by atomic force microscopy (AFM) in Figure S10a (Supporting Information), while a relatively smooth surface was obtained when CIP-200 nm was layered on top of the PIC-5  $\mu\text{m}$  in our designed SCE (Figure 5f; Figure S10b, Supporting Information). The large interfacial resistance due to poor contact with electrodes was addressed. The tensile strength of SCE was measured as 11.3 MPa, inheriting the good mechanical strength of PIC-5  $\mu\text{m}$ . The ionic conductivity of the SCE was  $2.3 \times 10^{-5} \text{ S cm}^{-1}$  at 30  $^{\circ}\text{C}$  and

$9.1 \times 10^{-5} \text{ S cm}^{-1}$  at 55  $^{\circ}\text{C}$ , respectively. It also fitted well with an Arrhenius plot. The electrochemical window of SCE is as high as 5.03 V due to the removal of impurities such as water from the interface by LLZTO particles (Figure S11, Supporting Information).

Even though the Li symmetric cell using the PIC-5  $\mu\text{m}$  electrolyte demonstrated stable cycling performance at 55  $^{\circ}\text{C}$ , the performance at 30  $^{\circ}\text{C}$  was a different case due to the interfacial issue explained above. As shown in Figure 6a, the PIC-5  $\mu\text{m}$  cell showed high overpotentials of 0.85–1.05 V and fluctuations starting from the initial cycles at 0.2  $\text{mA cm}^{-2}$  (0.1  $\text{mAh cm}^{-2}$ ). The cell soon reached a short circuit within 46 h. Note that the cell voltage recovered to normal Li-cycling potential after short circuit due to the passivated Li dendrite in electrolyte. The opposite galvanostatic electronic field drives the Li dendrite reverse growth, decreasing the length of dendrite. Once the Li in solid electrolytes becomes discrete, the cell voltage can recover after short circuit. The switching-off mechanism has been reported based on Ag dendrite.<sup>[28]</sup> The poor interfacial contact between PIC-5  $\mu\text{m}$  and Li metal can cause inhomogeneous current distribution and exacerbate the Li dendrite formation and growth.<sup>[16]</sup> As measured by EIS (Figure S12, Supporting Information), the interfacial resistance ( $R_f$ ) and charge-transfer resistance ( $R_{ct}$ ) for the PIC-5  $\mu\text{m}$  were 1825.7 and 1943.7  $\Omega \text{ cm}^2$ , respectively, much larger than those of the SCE ( $R_f$  of 511.7  $\Omega \text{ cm}^2$  and  $R_{ct}$  of 524.4  $\Omega \text{ cm}^2$ ). Our designed SCE enabled stable cycling performance over 400 h under 0.2  $\text{mA cm}^{-2}$  at 30  $^{\circ}\text{C}$ , which is almost ten times longer than the PIC-5  $\mu\text{m}$  cell (Figure 6b). As the EIS shown in Figure S13a (Supporting Information), the  $R_f$  and  $R_{ct}$  of SCE slightly increased to 521.4 and 531.8  $\Omega \text{ cm}^2$ , indicating a high electrochemical stability during long-term cycling. The SEM image exhibited a smooth surface of Li anode after cycling in Figure S13b (Supporting Information), which further confirmed the dendrite suppression capability of SCE.

The feasibility of SCE in full SSBs was investigated with a Li metal anode and an LFP cathode at 30  $^{\circ}\text{C}$ . The LFP cathode with succinonitrile (SCN) additive adopted the optimized composition from our previous work.<sup>[29]</sup> The initial impedance



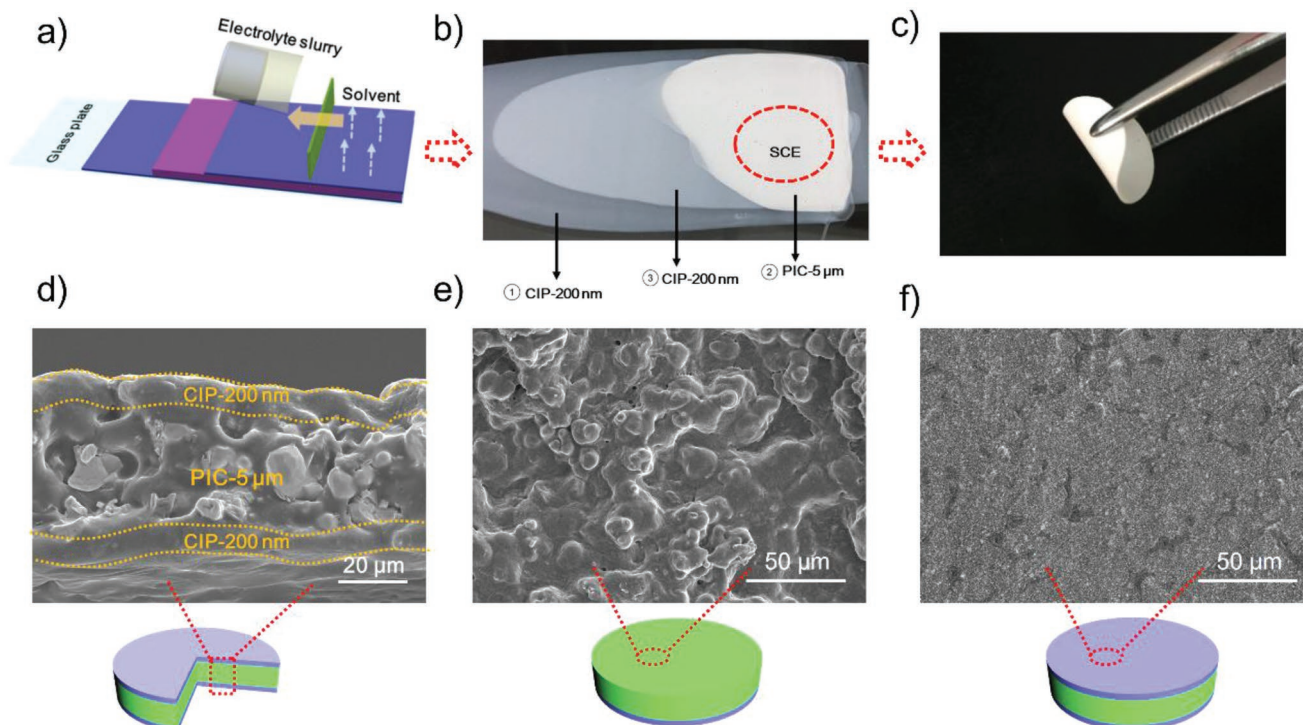


**Figure 5.** a) The schematic illustration of the SCE preparation by blade casting. Digital images of b) as-casted SCE on a glass plate and c) the bendable SCE. d) The cross-sectional SEM image of SCE with hierarchical structure (garnet particles with different sizes (200 nm and 5  $\mu\text{m}$ ) and contents (20 and 80 vol%) were orderly dispersed in the uniform polymer matrix). The top-view SEM images of e) PIC-5  $\mu\text{m}$  and f) SCE.

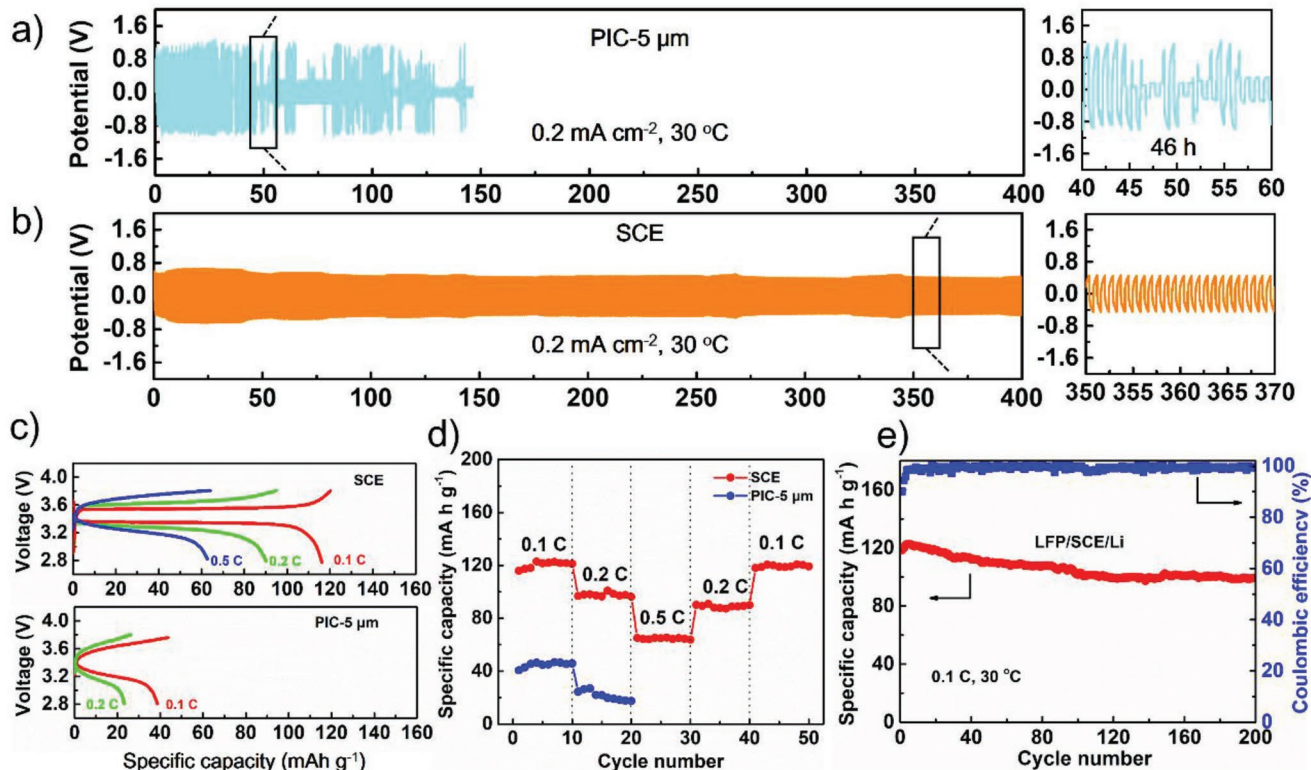


**Figure 6.** The voltage profiles of Li plating/stripping cycling with a) PIC-5  $\mu\text{m}$  electrolyte and b) SCE electrolyte cycling under 0.2  $\text{mA cm}^{-2}$  at 30  $^{\circ}\text{C}$ . c) The charge/discharge curves and d) rate performances of LFP/SCE/Li and LFP/PIC-5  $\mu\text{m}$ /Li cells at various current rates from 0.1 to 0.5 C. e) Cycling performance of the LFP/SCE/Li cell cycling under 0.1 C at 30  $^{\circ}\text{C}$ .

of the LFP/SCE/Li cell was  $2080.2 \Omega \text{ cm}^2$  at  $30^\circ \text{C}$ , which was only half of the value of the LFP/PIC-5  $\mu\text{m}$ /Li cell ( $4759.2 \Omega \text{ cm}^2$ ) (Figure S14, Supporting Information). The LFP/SCE/Li cell showed flat voltage plateaus with small polarization upon increasing current rates, unlike the severely polarized voltage profiles and significantly reduced specific capacity of the LFP/PIC-5  $\mu\text{m}$ /Li cell (Figure 6c). The SCE cell delivered an initial specific discharge capacity of  $118.6 \text{ mAh g}^{-1}$  and a Coulombic efficiency of 93.4% at 0.1 C. At higher current densities of 0.2 and 0.5 C, the SCE cell maintained specific capacities of 95.7 and  $63.2 \text{ mAh g}^{-1}$ , respectively (Figure 6d). When returning to 0.2 and 0.1 C after high-rate cycling, the specific capacity recovered to the similar level as before high-rate cycling. In great contrast, the cell with PIC-5  $\mu\text{m}$  delivered specific discharge capacities of merely 39.7 and  $20.6 \text{ mAh g}^{-1}$  at 0.1 and 0.2 C, respectively (Figure 6d). The low specific capacity and poor cycling stability could be attributed to the poor interfacial properties and uneven Li deposition. With the dendrite-suppressed SCE, the LFP/Li SSB can maintain a capacity retention of 82.4% after 200 cycles at 0.1 C at  $30^\circ \text{C}$  (Figure 6e). Our designed SCE has demonstrated great promise for building dendrite-free Li metal SSBs.

### 3. Conclusion

In summary, the dendrite-suppressing capability of composite electrolytes was investigated from “ceramic-in-polymer” to “polymer-in-ceramic” with different LLZTO concentrations and particle sizes. While the CIPs with smaller LLZTO particles showed higher ionic conductivities, the PICs with larger LLZTO particles exhibited better mechanical strength. A sandwich-type composite electrolyte with hierarchical LLZTO particles was rationally designed to achieve Li dendrite-free and good interfacial contacts at room temperature. The “polymer-in-ceramic” interlayer with 80 vol% 5  $\mu\text{m}$  LLZTO showed a high mechanical strength of 12.9 MPa, hindering Li dendrite propagation by physical obstacles. The “ceramic-in-polymer” thin-film outer layers with 20 vol% 200 nm LLZTO particles render a smooth and flexibility surface with a high  $t_+$  of 0.47. Li symmetric solid-state cells maintained highly stable plating/stripping cycling for 400 h under  $0.2 \text{ mA cm}^{-2}$  at  $30^\circ \text{C}$ . Full SSBs with the  $\text{LiFePO}_4$  cathode and Li metal anode delivered a room-temperature specific capacity of  $99.1 \text{ mAh g}^{-1}$  with a good capacity retention of 82.4% after 200 cycles at 0.1 C. Sandwich-type composite electrolytes with hierarchical fillers is a promising strategy to fabricate dendrite-free solid-state batteries with high energy density at room temperature. In addition, options of specific fillers and polymer matrixes can be versatile for to other electrolyte particles and polymers, which are expected to achieve the similar effects.

### 4. Experimental Section

**Materials Preparation:** PEO ( $M_n = 3 \times 10^5 \text{ g mol}^{-1}$ , Aladdin) was dried at  $60^\circ \text{C}$  overnight under vacuum prior to the electrolyte fabrication.  $\text{Li}_{6.4}\text{La}_3\text{Zr}_{1.4}\text{Ta}_{0.6}\text{O}_{12}$  (LLZTO) ceramic powders were prepared by the conventional solid-state reaction as described in the previous paper.<sup>[30]</sup> Crushed by planetary high-energy ball-milling, the particle size of the LLZTO

reduced from  $\approx 5 \mu\text{m}$  to 200 nm. Lithium bis(trifluoromethanesulfonyl) imide (LiTFSI) (99.95%, Sigma-Aldrich), anhydrous acetonitrile (ACN, Sigma-Aldrich), polyvinylidene fluoride (PVDF, Aladdin), super-conductive additives (SP, Timcal), LFP, and SCN were used as received.

**Fabrication of the Composite Electrolytes Containing LLZTO and PEO:** LLZTO particles with concentrations ranging from 20 to 80 vol% were added into ACN (25 mL) and dispersed by sonication to improve the dispersion. After that, PEO and LiTFSI (EO/Li<sup>+</sup> = 10:1 by mol) were added into the solution and stirred continuously for 8 h. Then, the homogenized colloidal solution was cast onto a glass plate with a controlled thickness. The ACN solvent was evaporated in a vacuum oven at  $60^\circ \text{C}$  for 12 h. The sandwich-type electrolytes were fabricated layer by layer using the same method. All procedures that are sensitive to moisture or oxygen were carried out in an Ar-filled glovebox (M-Braun, Germany) with  $\text{H}_2\text{O}$  and  $\text{O}_2$  levels below 0.1 ppm. In addition, the pure PEO(LiTFSI) membranes were also fabricated for comparison.

**Characterizations:** The X-ray diffraction was performed on the Bruker D2 Phaser with Cu K $\alpha$  radiation ( $\lambda = 1.5406 \text{ \AA}$ ) with  $2\theta$  range of  $10^\circ - 80^\circ$  and collected with a step-width of  $0.02^\circ$  at  $20^\circ \text{C}$  to characterize the crystalline structure of ingredients and synthesized membranes. The particle size distribution was tested by Zeta Plus (Brookhaven) laser particle size analyzer, using ethanol as the solvent and triethanolamine as the dispersant. The field emission scanning electron microscope (FESEM, Magellan 400) was employed to determine the morphologies of the surface and cross-section of all samples. The cross-sectional samples were obtained by liquid nitrogen quenching. All the samples for FESEM were coated with a thin layer of gold via sputtering. The modulus tests were conducted with a model 5948 MicroTester Instron instrument.

**Electrochemical Measurements and Cell Assembly:** The ionic conductivity of the SPEs was measured by the NOVOCONTROL spectrometer fitted with a temperature control system at varied temperatures from 30 to  $70^\circ \text{C}$ . The measurements were carried out in the frequency range from 0.01 Hz to 40 MHz. The stainless steel (SS) electrodes sandwiched the SPE to construct block/SPE/block cells. The electrochemical window was examined by SS/SPE/Li cells, using linear sweep voltammetry (LSV), which was conducted from 2 to 6 V at a scan rate of  $10 \text{ mV s}^{-1}$  by Arbin BT-2000. The lithium ion transference number was tested in a Li/SPE/Li cell (Autolab PGSTAT 302N system). The symmetric battery was polarized with a DC voltage of 10 mV. The AC impedance spectroscopy measurements before and after the polarization process were obtained. The LFP, LiTFSI, SP, PVDF, and SCN with an optimal weight ratio of LFP:LiTFSI:SP:PVDF = 10:7.5:2:1.5 and a molar ratio of SCN:LiTFSI = 7.5% were coated on Al foils to form the composite cathode.<sup>[29]</sup> The Li metal foil with a thickness of  $\approx 50 \mu\text{m}$  was used as the anodes. The 2032-type coin cells were assembled in an LFP/SCE/Li configuration. The cells were galvanostatically charged and discharged between 2.8 and 3.8 V versus Li/Li<sup>+</sup> under various current densities.

### Supporting Information

Supporting Information is available from the Wiley Online Library or from the author.

### Acknowledgements

The authors would like to thank the National Natural Science Foundation of China (Grant Nos. 51771222 and 51532002), the National Key R&D Program of China (Grant No. 2018YFB0104300), and the “Taishan Scholars Program.” H.H. thanks Dr. Ji Tan for SEM test and Dr. Chuang Yu for helpful discussions.

### Conflict of Interest

The authors declare no conflict of interest.

## Keywords

composite electrolytes, dendrite suppression, garnet particles, hierarchical structures, solid-state Li metal batteries

Received: December 28, 2018

Revised: February 25, 2019

Published online: March 7, 2019

- [1] a) J.-M. Tarascon, M. Armand, *Nature* **2001**, 414, 359; b) M. Armand, J.-M. Tarascon, *Nature* **2008**, 451, 652.
- [2] a) X. Yang, X. Li, K. Adair, H. Zhang, X. Sun, *Electrochem. Energy Rev.* **2018**, 1, 239; b) X. Li, X. Sun, *Adv. Funct. Mater.* **2018**, 28, 1801323; c) Y.-J. Wang, B. Fang, D. Zhang, A. Li, D. P. Wilkinson, A. Ignaszak, L. Zhang, J. Zhang, *Electrochem. Energy Rev.* **2018**, 1, 1.
- [3] Y. Zhao, K. Zheng, X. Sun, *Joule* **2018**, 2, 2583.
- [4] a) W. Xu, J. Wang, F. Ding, X. Chen, E. Nasybulin, Y. Zhang, J.-G. Zhang, *Energy Environ. Sci.* **2014**, 7, 513; b) Z. Peng, N. Zhao, Z. Zhang, H. Wan, H. Lin, M. Liu, C. Shen, H. He, X. Guo, J.-G. Zhang, D. Wang, *Nano Energy* **2017**, 39, 662.
- [5] a) M. He, Z. Cui, C. Chen, Y. Li, X. Guo, *J. Mater. Chem. A* **2018**, 6, 11463. b) J. Ju, Y. Wang, B. Chen, J. Ma, S. Dong, J. Chai, H. Qu, L. Cui, X. Wu, G. Cui, *ACS Appl. Mater. Interfaces* **2018**, 10, 13588.
- [6] K. K. Fu, Y. Gong, J. Dai, A. Gong, X. Han, Y. Yao, C. Wang, Y. Wang, Y. Chen, C. Yan, *Proc. Natl. Acad. Sci. USA* **2016**, 113, 7094.
- [7] P. V. Wright, *Polym. Int.* **1975**, 7, 319.
- [8] C. W. Liew, R. Durairaj, S. Ramesh, *PLoS One* **2014**, 9, e102815.
- [9] W. H. Meyer, *Adv. Mater.* **1998**, 10, 439.
- [10] K. Vignarooban, M. Dissanayake, I. Albinsson, B.-E. Mellander, *Solid State Ionics* **2014**, 266, 25.
- [11] a) C. W. Lin, C. L. Hung, M. Venkateswarlu, B. J. Hwang, *J. Power Sources* **2005**, 146, 397; b) D. Lin, W. Liu, Y. Liu, H. R. Lee, P. C. Hsu, K. Liu, Y. Cui, *Nano Lett.* **2016**, 16, 459.
- [12] J. Zhang, N. Zhao, M. Zhang, Y. Li, P. K. Chu, X. Guo, Z. Di, X. Wang, H. Li, *Nano Energy* **2016**, 28, 447.
- [13] a) S. Chen, Y. Zhao, J. Yang, L. Yao, X. Xu, *Ionics* **2016**, 23, 2603; b) Z. Wan, D. Lei, W. Yang, C. Liu, K. Shi, X. Hao, L. Shen, W. Lv, B. Li, Q. H. Yang, *Adv. Funct. Mater.* **2019**, 29, 1970006.
- [14] C. Z. Zhao, X. Q. Zhang, X. B. Cheng, R. Zhang, R. Xu, P. Y. Chen, H. J. Peng, J. Q. Huang, Q. Zhang, *Proc. Natl. Acad. Sci. USA* **2017**, 114, 11069.
- [15] C. Monroe, J. Newman, *J. Electrochem. Soc.* **2005**, 152, A396.
- [16] X. Han, Y. Gong, K. K. Fu, X. He, G. T. Hitz, J. Dai, A. Pearse, B. Liu, H. Wang, G. Rubloff, Y. Mo, V. Thangadurai, E. D. Wachsman, L. Hu, *Nat. Mater.* **2017**, 16, 572.
- [17] a) X. Sun, J. Liang, Q. Sun, Y. Zhao, Y. Sun, C. Wang, W. Li, M. Li, D. Wang, X. Li, *J. Mater. Chem. A* **2018**, 6, 23712; b) S. Xu, D. W. McOwen, C. Wang, L. Zhang, W. Luo, C. Chen, Y. Li, Y. Gong, J. Dai, Y. Kuang, *Nano Lett.* **2018**, 18, 3926.
- [18] Y. Gong, K. Fu, S. Xu, J. Dai, T. R. Hamann, L. Zhang, G. T. Hitz, Z. Fu, Z. Ma, D. W. McOwen, *Mater. Today* **2018**, 21, 594.
- [19] a) F. Du, N. Zhao, Y. Li, C. Chen, Z. Liu, X. Guo, *J. Power Sources* **2015**, 300, 24; b) Y. Li, Z. Wang, C. Li, Y. Cao, X. Guo, *J. Power Sources* **2014**, 248, 642.
- [20] P. Reschiglian, G. Torsi, *Chromatographia* **1995**, 40, 467.
- [21] H. Huo, J. Sun, C. Chen, X. Meng, M. He, N. Zhao, X. Guo, *J. Power Sources* **2018**, 383, 150.
- [22] a) W. Wang, E. Yi, A. J. Fici, R. M. Laine, J. Kieffer, *J. Phys. Chem. C* **2017**, 121, 2563; b) H. Yamada, A. J. Bhattacharyya, J. Maier, *Adv. Funct. Mater.* **2006**, 16, 525.
- [23] L. Chen, Y. Li, S.-P. Li, L.-Z. Fan, C.-W. Nan, J. B. Goodenough, *Nano Energy* **2018**, 46, 176.
- [24] S. Yu, R. D. Schmidt, R. Garcia-Mendez, E. Herbert, N. J. Dudney, J. B. Wolfenstine, J. Sakamoto, D. J. Siegel, *Chem. Mater.* **2015**, 28, 197.
- [25] J. Zhang, J. Zhao, L. Yue, Q. Wang, J. Chai, Z. Liu, X. Zhou, H. Li, Y. Guo, G. Cui, L. Chen, *Adv. Energy Mater.* **2015**, 5, 1501082.
- [26] Z. Xue, D. He, X. Xie, *J. Mater. Chem. A* **2015**, 3, 19218.
- [27] H. Huo, N. Zhao, J. Sun, F. Du, Y. Li, X. Guo, *J. Power Sources* **2017**, 372, 1.
- [28] X. Guo, C. Schindler, S. Menzel, R. Waser, *Appl. Phys. Lett.* **2007**, 91, 133513.
- [29] M. He, Z. Cui, F. Han, X. Guo, *J. Alloys Compd.* **2018**, 762, 157.
- [30] Y. Li, Y. Cao, X. Guo, *Solid State Ionics* **2013**, 253, 76.